RADIATION RESEARCH **176,** 587–602 (2011)
0033-7587/11 $15.00

DOI: 10.1667/RR2663.1

Effects of Radiation Quality and Oxygen on Clustered DNA Lesions and Cell Death

Robert D. Stewart,[a,1] Victor K. Yu,[b,c] Alexandros G. Georgakilas,[d] Constantinos Koumenis,[e] Joo Han Park[c] and David J. Carlson[b]

[a] *Department of Radiation Oncology, University of Washington, Seattle, Washington 98195-6043;* [b] *Department of Therapeutic Radiology, Yale University School of Medicine, New Haven, Connecticut 06520-8040;* [c] *School of Health Sciences, Purdue University, West Lafayette, Indiana 47907-2051;* [d] *Department of Biology, Thomas Harriot College of Arts and Sciences, East Carolina University, Greenville, North Carolina 27858-4353; and* [e] *University of Pennsylvania School of Medicine, Department of Radiation Oncology, Philadelphia, Pennsylvania 19104-6072*

Stewart, R. D., Yu, V. K., Georgakilas, A. G., Koumenis, C., Park, J. H. and Carlson, D. J. Effects of Radiation Quality and Oxygen on Clustered DNA Lesions and Cell Death. *Radiat. Res.* 176, 587–602 (2011).

Radiation quality and cellular oxygen concentration have a substantial impact on DNA damage, reproductive cell death and, ultimately, the potential efficacy of radiation therapy for the treatment of cancer. To better understand and quantify the effects of radiation quality and oxygen on the induction of clustered DNA lesions, we have now extended the Monte Carlo Damage Simulation (MCDS) to account for reductions in the initial lesion yield arising from enhanced chemical repair of DNA radicals under hypoxic conditions. The kinetic energy range and types of particles considered in the MCDS have also been expanded to include charged particles up to and including ^{56}Fe ions. The induction of individual and clustered DNA lesions for arbitrary mixtures of different types of radiation can now be directly simulated. For low-linear energy transfer (LET) radiations, cells irradiated under normoxic conditions sustain about 2.9 times as many double-strand breaks (DSBs) as cells irradiated under anoxic conditions. New experiments performed by us demonstrate similar trends in the yields of non-DSB (Fpg and Endo III) clusters in HeLa cells irradiated by γ rays under aerobic and hypoxic conditions. The good agreement among measured and predicted DSBs, Fpg and Endo III cluster yields suggests that, for the first time, it may be possible to determine nucleotide-level maps of the multitude of different types of clustered DNA lesions formed in cells under reduced oxygen conditions. As particle LET increases, the MCDS predicts that the ratio of DSBs formed under normoxic to hypoxic conditions by the same type of radiation decreases monotonically toward unity. However, the relative biological effectiveness (RBE) of higher-LET radiations compared to ^{60}Co γ rays (0.24 keV/μm) tends to increase with decreasing oxygen concentration. The predicted RBE of a 1 MeV proton (26.9 keV/μm) relative to ^{60}Co γ rays for DSB induction increases from 1.9 to 2.3 as oxygen concentration decreases from 100% to 0%. For a 12 MeV ^{12}C ion (681 keV/μm), the predicted RBE for DSB induction increases from 3.4 (100% O_2) to 9.8 (0% O_2). Estimates of linear-quadratic (LQ) cell survival model parameters (α and β) are closely correlated to the Monte Carlo-predicted trends in DSB induction for a wide range of particle types, energies and oxygen concentrations. The analysis suggests α is, as a first approximation, proportional to the initial number of DSBs per cell, and β is proportional to the square of the initial number of DSBs per cell. Although the reported studies provide some evidence supporting the hypothesis that DSBs are a biologically critical form of clustered DNA lesion, the induction of Fpg and Endo III clusters in HeLa cells irradiated by γ rays exhibits similar trends with oxygen concentration. Other types of non-DSB cluster may still play an important role in reproductive cell death. The MCDS captures many of the essential trends in the formation of clustered DNA lesions by ionizing radiation and provides useful information to probe the multiscale effects and interactions of ionizing radiation in cells and tissues. Information from Monte Carlo simulations of cluster induction may also prove useful for efforts to better exploit radiation quality and reduce the impact of tumor hypoxia in proton and carbon-ion radiation therapy.

INTRODUCTION

Many decades of biophysical research (*1–4*) provide evidence suggesting that the number and spatial arrangement of energy deposits within and near the DNA have an impact on mutagenesis, chromosomal aberrations and cell death. Through a breakage and reunion process, double-strand breaks (DSBs) are converted to small- and larger-scale chromosomal exchanges with the potential to cause phenotypic alterations, neoplasia and cell death (*2*). Other types of non-DSB cluster may also have significant biological consequences (*5*, *6*). Although molecular and cellular processes may sometimes negate, amplify or suppress the effects of initial DNA damage, trends in DSB induction with radiation quality are often quite similar to trends in the numbers of lethal events per unit dose

---

[1] Address for correspondence: University of Washington, Department of Radiation Oncology, University Cancer Center, UWMC, 1959 NE Pacific Street, Box 356043, Seattle, WA 98195-6043; trawets@uw.edu.

arising from individual particles with a linear energy transfer (LET) of less than 100 keV/μm (*7*). Reductions in the initial DSB yield with decreasing oxygen concentration are also consistent with increases in cell survival under hypoxic relative to normoxic conditions (*8*). However, local cluster complexity may also have an impact on higher-level biological end points (*1*, *4*), and very little is known about the effects of hypoxia on the local complexity of DSB and non-DSB clusters. As the only method currently available to determine the number and spatial configuration of lesions forming a cluster, Monte Carlo simulations are a potentially useful adjunct to experiments probing the underlying basis for the effects of oxygen and radiation quality on cell death. Estimates of DSB yields from Monte Carlo simulations can also be used in combination with kinetic reaction-rate models, such as the repair-misrepair-fixation (RMF) model (*7*), to determine the relative biological effectiveness (RBE) of different types of radiation for cell killing. An improved understanding of RBE and oxygen effects is needed to more fully exploit the biological potential of protons and carbon ions in radiation therapy (*9*, *10*), especially since high levels of pretreatment tumor hypoxia have been implicated as a significant factor contributing to treatment failure (*11*).

Radiation creates DNA lesions through the direct deposition of energy in the DNA as well as through the indirect action of reactive chemical species formed near the DNA (*3*). Indirect damage is primarily attributed to the formation of hydroxyl radicals ($^{\cdot}$OH) through the radiolysis of water near (<∼10 nm) the DNA (*3*). The average diffusion distance of an $^{\cdot}$OH in a cellular milieu is about 6 nm (*12*), or about three times the diameter of the DNA double helix, which implies that the chance an $^{\cdot}$OH formed through the radiolysis of water will interact with a nucleotide in DNA decreases rapidly with distance beyond about 4 to 6 nm. Electrons and other low-LET radiations create about 217 strand breaks Gy^{-1} Gbp^{-1} and about 650 damaged bases (including abasic sites) Gy^{-1} Gbp^{-1} (*13*), i.e., a ratio of about 3 damaged bases per strand break (*4*). For low-LET radiations, about 50% of the lesions arise from unscavengeable (direct or indirect) mechanisms and the remaining lesions are scavengeable (*13*). Because energy deposition is proportional to mass, the purines (adenine and guanine) and pyrimidines (cytosine and thymine) are about equally likely to sustain damage through the direct mechanism. All four types of DNA base are about equally sensitive to $^{\bullet}$OH attack (*3*).

For normal human fibroblasts (MRC-5), Rothkamm and Löbrich (*14*) have shown that the number of γ-H2AX foci, a surrogate for the initial number of DSBs per cell, is proportional to absorbed dose in the range from 1 mGy to 2 Gy. Pulsed-field gel electrophoresis (PFGE) measurements also demonstrate that DSB induction in MRC-5 cells is proportional to absorbed dose from 10 to 80 Gy (*14*). In human fibroblasts, DSB induction is proportional to absorbed dose up to 700 Gy for protons and α particles (*15*). Prise *et al.* (*16*) compiled data from a large number of experimental studies on DSB induction by ionizing radiation in various types of eukaryotic cells. DSB yields measured using the PFGE assay, when expressed per unit genome length, are similar among yeast and mammalian cells despite order-of-magnitude differences in genome sizes (all reported estimates are in the range from 4.2 to 6.9 DSBs Gy^{-1} Gbp^{-1}). This observation suggests that DSB induction per base pair is approximately the same in the lower and higher eukaryotes. In yeast cells irradiated by 30 MeV electrons, the initial DSB yield per cell increases linearly with dose up to at least 2400 Gy under fully aerobic (100% O_2) conditions and up to at least 1500 Gy under maximally hypoxic conditions (*17*). The production of Fpg (oxidized purine), Endo III (oxidized pyrimidine) and Endo IV (abasic) non-DSB clusters is also proportional to absorbed dose for low- and high-LET radiations from at least 0.05 Gy up to 30 Gy (*6*, *18–23*). Collectively, these experimental observations provide compelling evidence that the induction of DSBs and other non-DSB clusters is proportional to absorbed dose up to at least several hundred Gy under normoxic and hypoxic conditions. These observations also imply that, for the clinically relevant range of absorbed doses (i.e., doses <200 Gy), all of the initial clustered DNA lesions formed by ionizing radiation, including DSBs, are formed predominately through single-hit (one-track) mechanisms regardless of oxygen concentration.

In a normoxic environment, the initial DNA radicals formed through direct or indirect damage mechanisms may interact with O_2, endogenous thiols such as glutathione, or other cellular constituents. The reduction of DNA radicals by thiols has been termed *chemical repair* [reviewed in ref. (*24*)]. In competition with chemical repair, the interaction of a DNA radical with oxygen, a process termed *oxygen fixation*, creates a peroxy radical that must be processed by enzymatic mechanisms, such as base excision repair (BER), to restore the integrity of the DNA double helix. BER is the primary mechanism for the removal of clustered DNA lesions other than the DSB (*25*, *26*). In mammalian cells, non-homologous end joining (NHEJ) is responsible for most DSB rejoining (*27*, *28*), although homologous recombination (HR) contributes to DSB repair during the S and G_2 phases (*29*, *30*). The interaction of a DNA radical with nearby undamaged nucleotides or with other cellular constituents may also produce a crosslink requiring enzymatic processing to restore DNA integrity. Regardless, the net effect on cluster induction of irradiating cells under reduced oxygen is to enhance opportunities for chemical repair and thus decrease the numbers of individual and clustered DNA lesions, including DSBs (*31–37*), processed by enzymatic repair mechanisms.

Comparisons of the effects of low- and high-linear energy transfer (LET) radiations (*1*, *32*, *38–40*) suggest that repair tends to decrease and biological consequences tend to increase as the induction of damage by radiation shifts from clusters composed of small numbers of lesions (low-LET radiation) to clusters composed of many lesions (high-LET radiation). The experimentally observed reductions in the initial DSB yield detected in cells under reduced oxygen conditions (*1*, *32*, *38–40*) suggest that the average number of lesions per cluster, a measure of *cluster complexity*, tends to decrease as oxygen concentration decreases. If true, the decreased (average) complexity of the clusters formed under reduced oxygen conditions may enhance the accuracy of cluster repair. For end points such as chromosomal aberrations (*41*, *42*) and cell death (*32*, *33*, *36*, *39*, *43–57*), the decreased sensitivity of hypoxic cells to ionizing radiation may be due in part to an increase in the accuracy of repair as well as to a reduction in the initial number of clusters a cell must repair.

In this article, we develop a Monte Carlo model to estimate the yields of clustered DNA lesions formed by ionizing radiation under conditions of reduced oxygen. The kinetic energy range and types of particles considered in the Monte Carlo Damage Simulation[2] (MCDS) are also expanded to include ions up to and including ^{56}Fe. As a first step toward validation of the extended MCDS, calculated yields of DSBs and other types of clustered DNA lesions are compared to measured data for photons and selected intermediate- and high-LET radiations. The reported studies provide new information to better quantify the effects of oxygen on the initial yield and complexity of the multitude of different types of clustered DNA lesions formed by ionizing radiation.

MATERIALS AND METHODS

Monte Carlo Simulation of Individual and Clustered DNA Lesions

The published MCDS (*13*, *58*) simulates the induction and clustering of DNA lesions in normoxic cells (O_2 concentrations greater than about 21%) uniformly irradiated by monoenergetic electrons (>80 eV), protons (>0.105 MeV) and α particles (>2 MeV) with energies as high as 1 GeV. In the new MCDS (version 3.0), the allowed particle types have been expanded to include ions up to and including ^{56}Fe. The software has also been extended so that the induction of damage can be simulated for arbitrary mixtures of charged particles with the same or different kinetic energies.

1. Specification of radiation quality

The ratio of the square of the effective charge and the square of the particle's speed relative to the speed of light in a vacuum, $(Z_{eff}/\beta)^2$, is used in the MCDS as the preferred indicator of radiation quality. The effective charge of a positive or negative ion is calculated according to Barkas and Evans (*59*) as

$$Z_{eff} = Z[1 - \exp(125 \cdot \beta \cdot Z^{-2/3})], \tag{1}$$

and β is given by

$$\beta = \sqrt{1 - \frac{1}{(1 + T/m_0c^2)^2}}. \tag{2}$$

Here, T is the kinetic energy of the charged particle, and m_0c^2 is the rest mass energy of the charged particle. For ions with $Z > 2$, simulation parameters are assumed the same for all ions with the same $(Z_{eff}/\beta)^2$, as in version 2.0 of the MCDS (*13*, *58*). Table 1 lists the minimum kinetic energy allowed in MCDS Version 3.0 for selected ions, i.e., energies corresponding to $(Z_{eff}/\beta)^2 \leq 10{,}000$. In MCDS 2.0 (*13*), simulations were restricted to electrons, protons and α particles with $(Z_{eff}/\beta)^2 \leq 3{,}200$.

Although not required for the simulation of damage induction, the MCDS also reports charged-particle stopping power in liquid water as a secondary indicator of radiation quality. For monoenergetic electrons, protons and α particles with kinetic energies greater than 10 keV, stopping powers in liquid water are based on an empirical fit to data from the National Institute of Standards and Technology (NIST) STAR database (http://www.nist.gov/physlab/data/star/). For electrons with kinetic energies below 10 keV, collisional stopping powers in liquid water are based on an empirical fit to data from the IXS-D3 model of Emfietzoglou and Nikjoo (*60*). For $Z > 2$, charged-particle stopping power in water is equated to the stopping power of an α particle with the same $(Z_{eff}/\beta)^2$. For photons, the MCDS computes a fluence-averaged stopping power from the spectrum of secondary electrons arising when the (primary) photon first interacts in or near the cell nucleus (*61*, *62*). The MCDS also has the capability to estimate the fluence-averaged stopping power for a mixture of ions with the same or different kinetic energy.

For a target (cell nucleus) with input diameter d, the MCDS automatically tabulates microdosimetric parameters, such as the frequency-mean specific energy ($\bar{z}_F$) and lineal energy $\bar{y}_F$ (*63*), the absorbed dose per unit fluence [$D/\Phi = \pi d^2 \bar{z}_F/4$], and the average path length R traveled by a charged particle as it slows down, as calculated using the continuous-slowing-down approximation (i.e., the CSDA range). Estimates of the CSDA range and microdosimetric quantities reported by the MCDS are provided for conceptual purposes and as secondary indicators of radiation quality; estimates of these quantities do not have *any* impact on the Monte Carlo simulation of DNA damage induction within the MCDS. In the MCDS, the frequency-mean specific energy (in Gy) is approximated as $\bar{z}_F = 0.3059\overline{\Delta E}/\rho d^3$. Here, $\overline{\Delta E}$ is the average energy deposited (in keV) by ions passing through a target with density ρ (g cm^{-3}) and diameter d (in μm). The average energy deposited in the target is the integral of the chord length l times the stopping power weighted by the relative number of particles traveling distance l, i.e.,

$$\overline{\Delta E} = \int_0^{\min(R,d)} dl\, l f(l)[S(l) - S_{rad}(l)]. \tag{3}$$

Here, $f(l)dl$ is the fraction of the particles traveling distance l to $l + dl$ with collisional (electronic) and nuclear stopping power $S(l) - S_{rad}(l)$. Radiative energy losses (S_{rad}) are assumed to be non-local because the mean free path length of a photon is typically very large compared to the dimensions of the cell nucleus. The integral is from 0 to min(R, d) to ensure that the energy deposited in the target of interest does not exceed the particle's kinetic energy. For a spherical body exposed to a uniform isotropic fluence of particles traveling in straight lines, sometimes referred to as μ-randomness, the distribution of chord lengths is given by $f(l) = 2l/d^2$ (*64*), and Eq. (3) becomes

$$\overline{\Delta E} = \left(\frac{2}{d^2}\right) \int_0^{\min(R,d)} dl\, l^2[S(l) - S_{rad}(l)]. \tag{4}$$

For the special case when $S - S_{rad}$ (in keV/μm) is constant while the particle passes through a target, Eq. (4) reduces to

$$\overline{\Delta E} = \frac{2d}{3}[S - S_{rad}] \tag{5}$$

and the frequency-mean specific energy (in Gy) is

$$\bar{z}_F = 0.204[S - S_{rad}]/\rho d^2. \tag{6}$$

---

[2] An executable version of the MCDS software is available at http://faculty.washington.edu/trawets/mcds/.

TABLE 1
Minimum Allowed Kinetic Energy (KE) and Related Properties of Selected Ions in Water as Reported by the MCDS

	Kinetic energy				$\bar{z}_F$ (Gy)	
Particle type	MeV	MeV/u	$S - S_{rad}$ (keV/μm)	CSDA range (μm)	MCDS	Eq. (6)
e^-	2.56×10^{-5}	-	21.13	2×10^{-3}	$<10^{-11}$	0.17
^{1}H	6.47×10^{-3}	6.47×10^{-3}	34.2	0.28	$<10^{-4}$	0.29
$^3He^{2+}$	0.222	7.39×10^{-2}	186	2.03	0.06	1.53
$^4He^{2+}$	0.294	7.35×10^{-2}	186	2.70	0.14	1.53
$^{12}C^{6+}$	14.8	1.23	612	21.13	5.32	5.08
$^{14}N^{7+}$	24.7	1.76	663	30.42	5.68	5.49
$^{16}O^{8+}$	38.1	2.38	711	42.03	6.01	5.86
$^{20}Ne^{10+}$	78.4	3.92	792	73.14	6.60	6.50
$^{56}Fe^{26+}$	1750	31.3	1148	963.7	9.35	9.34

Notes. The minimum KE is equivalent to $(Z_{eff}/\beta)^2 = 10{,}000$. Estimates of $\bar{z}_F$, the frequency-mean specific energy, are for a representative cell nucleus 5 μm in diameter. S is the total stopping power, and S_{rad} is the radiative stopping power.

As illustrated by the estimates of the frequency-mean specific energy tabulated in Table 1, Eq. (6) is only a good approximation for $\bar{z}_F = 0.3059\overline{\Delta E}/\rho d^3$ when the CSDA range is large compared to the diameter of the cell nucleus. As the CSDA range becomes comparable to the dimensions of the nucleus, changes in the stopping power of the ion while passing through the target become significant. When the range of an ion becomes smaller than the diameter of the nucleus, the average energy deposited by a particle decreases rapidly because the ion may stop (lose all kinetic energy) before passing through the target. The effects of such stoppers are included in Eq. (4) by integrating from 0 to min(R, d) whereas, in Eq. (6), the effects of stoppers are neglected. When $R < d$, estimates of the frequency-mean specific energy reported by the MCDS may be much less than the mean specific energy computed using the more approximate, analytical formula [Eq. (6)]. Although the formulas and algorithms used in the MCDS to estimate microdosimetric quantities account for changes in stopping power within the target, other potentially important physical processes, such as δ-ray escape and pathlength straggling (*63*, *65*), are neglected. Pathlength straggling, which tends to increase energy deposition within a target, is especially important for lower-energy electrons. The significance of δ-ray escape, which effectively reduces energy deposition within the target, increases as the kinetic energy of the ion increases.

2. *Damage simulation for well-oxygenated cells*

The algorithm used in the MCDS to simulate the induction of individual and clustered DNA lesions has been described in detail elsewhere (*13*, *58*). Briefly, damage simulations in well oxygenated cells are performed in two major steps: (1) randomly distribute in a DNA segment the expected number of lesions produced in a cell per Gy of radiation and (2) subdivide the lesions in the segment into clusters. DNA segment length is given by a parameter n_{seg} expressed in units of base pairs (bp) Gy^{-1} $cell^{-1}$. This segment length is an *ad hoc* parameter and should not be considered equivalent to the DNA content of a specific chromosome or cell. The number of lesions to be distributed within the segment is given by the sum of the number of strand breaks Gy^{-1} $cell^{-1}$, σ_{Sb}, and the number of base damages Gy^{-1} $cell^{-1}$, $\sigma_{Bb} = f\sigma_{Sb}$, where f is the base damage to strand break ratio. Finally, the grouping of lesions into clusters is determined by a parameter N_{min} (bp), which specifies the minimum length of undamaged DNA between neighboring lesions such that these lesions are said to belong to two different clusters (some "clusters" may contain only one lesion). The MCDS algorithm thus has four adjustable parameters: n_{seg}, σ_{Sb}, f and N_{min}. For well-oxygenated cells with a DNA content of 6 Gbp, the default (*recommended*) parameters used in the MCDS are $\sigma_{Sb} = 1{,}300$ Gy^{-1} $cell^{-1}$ (216.7 Gy^{-1} Gbp^{-1}), $f = 3$, $N_{min} = 9$ bp, and $n_{seg}(x) = 149{,}200 - 123{,}600x/(x+267)$, where $x \equiv (Z_{eff}/\beta)^2$ (*13*).

3. *Simulation of the effects of chemical repair and oxygen fixation*

To simulate the effects of oxygen on the formation of individual and clustered DNA lesions within the MCDS, a three-step algorithm is proposed:

Step 1. Simulate the number and location within the DNA of individual and clustered DNA radicals using the published MCDS algorithm (*13*, *58*). By using the existing algorithm to simulate the initial location of DNA radicals, the radical and lesion clustering effects arising from the structure of individual particle tracks are preserved (i.e., the same as in the original MCDS).

Step 2. Determine the probability a DNA radical is reduced, for example, by a thiol within the cellular environment rather than fixed by O_2 (i.e., the *oxygen fixation hypothesis*). The fraction of the initial DNA radicals removed through the chemical repair process is determined using the formula:

$$p_R(x, [O_2]) = 1 - \frac{[O_2] + K}{[O_2] + M(x) \cdot K}. \tag{7}$$

Here, $[O_2]$ denotes the % O_2 concentration at the time of irradiation, the quantity $(1 - 1/M)$ represents the maximum fraction of DNA radicals removed through chemical repair under fully anoxic conditions, K is the % oxygen concentration at which half of the maximum is removed, and $x \equiv (Z_{eff}/\beta)^2$. To account for factors that reduce the effectiveness of chemical repair as $(Z_{eff}/\beta)^2$ increases, such as increased radical clustering or other chemical modifications to the DNA, $M(x)$ is modeled using the empirical formula:

$$M(x) = M_0 - \frac{(M_0 - 1)}{1 + (q/x)^r}. \tag{8}$$

Here, M_0, q and r are adjustable parameters that capture essential physiochemical factors and processes that hamper the chemical repair process *in vitro* or *in vivo*. Here, M_0 determines the maximum fraction of the DNA radicals that can be removed through chemical repair, and the term involving the ratio q/x corrects for changes in the effectiveness of chemical repair with radiation quality. For low-LET radiations, q/x is large, oxygen fixation is minimized and chemical repair is maximized. In the limit as q becomes very large compared to $x = (Z_{eff}/\beta)^2$, $M(x)$ approaches the asymptotic value M_0. As particle LET increases, q/x decreases, $M(x)$ approaches unity, and oxygen fixation is maximized (i.e., a well-oxygenated cellular environment).

Step 3. Remove fraction $p_R(x,[O_2])$ of the DNA radicals created in *step 1*. As a working hypothesis, we assume that all of the initial DNA radicals created in *step 1* are equally likely to be removed through the chemical repair process. This hypothesis implies that all of the initial DNA radicals forming a putative cluster are equally accessible to O_2 and to DNA radical scavengers in the cellular environment. Also, the interaction kinetics among DNA radicals, scavengers and O_2 is assumed not to saturate. These assumptions imply that the chemical removal of individual DNA radicals is monoexponential (first-order chemical repair). For clusters of 2 or more DNA radicals, chemical repair kinetics may appear to be mono- or multiexponential. In gas explosion experiments, Prise *et al.* (*66*, *67*) found that the precursors to SSBs and DSBs exhibited exponential repair kinetics.

4. Simulation of clusters from photons

Although the MCDS does not have the ability to directly simulate cluster yields for photons or other neutral particles, secondary electron spectra for ^{60}Co and ^{137}Cs in a monolayer cell geometry (*61*) were used to generate spectrum-averaged cluster yields. For the other photon sources considered in this work (50, 200, 250, 270 and 280 kVp and 10 MV X rays), we used the Monte Carlo N-Particles Transport Code (MCNP) Version 5.140 to generate secondary electron spectra in a monolayer cell culture geometry comparable to the one used in Hsiao and Stewart (*61*). Simulations for kilovoltage X rays included a 0.5-mm Cu and 4-mm Al filter. MCNP-generated secondary electron spectra are based on a minimum of 10^7 particle histories. A 1 keV photon and electron cutoff energy was used for all MCNP simulations. Differences among DSB yields for ^{60}Co, ^{137}Cs and filtered 220 kVp X rays computed using electron spectra generated using PENELOPE (*61*) and MCNP were negligible ($<1\%$).

Analysis of Published Data Sets

In many published studies, the oxygen enhancement ratio (OER) is used to quantify the effects of oxygen on DNA damage, cell killing and other biological end points. The OER is usually defined as the ratio of the absorbed dose required to produce biological effect E (e.g., a given level of cell killing) under maximally hypoxic conditions to the absorbed dose required to produce the same effect E under normoxic conditions. Alternatively, many groups (*8*, *68–73*) have used the OER as a scaling factor to determine the radiation sensitivity of cells irradiated under reduced oxygen. However, the use of the OER as a scaling factor for radiation sensitivity parameters often produces trends counter to ones associated with the traditional definition of an OER. Because radiation sensitivity parameters are more often known for normoxic conditions than hypoxic conditions and because of the sometimes inconsistent use of the OER term in the literature, we prefer, and will henceforth use, the term *hypoxia reduction factor* (*HRF*) rather than OER to quantify the effects of oxygen concentration on DNA damage and other biological end points. Because of the close relationship between DSB induction and clonogenic survival (*7*), estimates of the *HRF* derived from clonogenic survival data are used to supplement data from direct measurements of DSBs and other cluster yields.

1. HRF for individual and clustered DNA lesions

Formally, the *HRF* is the ratio of the absorbed dose required to produce biological effect E under maximally hypoxic conditions to the absorbed dose required to produce the same effect E under normoxic conditions. Because the induction of DNA damage is proportional to absorbed dose up to at least a few hundred Gy of low- or high-LET radiation regardless of oxygen concentration (*15*, *31*), the *HRF* for DSB induction, HRF_{dsb}, can be expressed as a ratio of doses or as a ratio of DSB yields, i.e.,

$$HRF_{dsb}([\mathrm{O}_2]) = \frac{D([\mathrm{O}_2])}{D_N} = \frac{\Sigma_N}{\Sigma([\mathrm{O}_2])}. \qquad (9)$$

Here, D_N is the absorbed dose required to produce σ_N DSB (Gy^{-1} Gbp^{-1}) in cells irradiated under normoxic conditions, and $D([\mathrm{O}_2])$ is the absorbed dose required to produce $\sigma([\mathrm{O}_2])$ DSB (Gy^{-1} Gbp^{-1}) in cells irradiated under oxygen concentration $[\mathrm{O}_2]$. An equation mathematically equivalent to Eq. (9) is also appropriate for other types of individual of clustered DNA lesion. For biological end points, such as reproductive cell survival, with non-linear dose–response characteristics, alternate *HRF* formulas must be derived from isoeffect relationships, e.g., see ref. (*8*).

2. HRF for clonogenic cell survival

The survival of cells irradiated under varying oxygen concentrations is well approximated by the linear-quadratic (LQ) cell survival model; i.e., the fraction S of the cells surviving absorbed dose D is $S \cong \exp(-\alpha D - \beta G D^2)$. Here, α and β characterize intrinsic cellular radiation sensitivity and G is the dose protraction factor. The dose protraction factor is a correction to the intertrack (dose-squared) term that accounts for the temporal pattern of radiation delivery, including dose-rate and dose-fractionation effects in radiation therapy. For a single dose of radiation delivered at constant dose rate during time interval T, G is given by $G(x) = 2(e^{-x} + x - 1)/x^2$, where $x \equiv \mathrm{T} \ln 2/\tau$. Here, τ is the effective half-time for sublethal damage repair. A number of published studies have demonstrated that the effects of oxygen on cell survival can be incorporated into the LQ by modifying α and β by dimensionless factors HRF_α and HRF_β, respectively. That is, the LQ survival model for reduced oxygen concentrations becomes $S \cong \exp[-(\alpha_N/HRF_\alpha)D - (\beta_N/HRF_\beta)GD^2]$. As a close approximation, $HRF_\alpha \cong (HRF_\beta)^{1/2} = HRF$ (*8*) and the surviving fraction becomes $S \cong \exp[-(\alpha_N/HRF)D - (\beta_N/HRF^2)GD^2]$.

As in Carlson *et al.* (*8*), we performed simultaneous three-parameter fits (α_N, β_N and *HRF*) to published cell survival data for mammalian cells exposed *in vitro* to particles with widely varying radiation quality under normoxic and reduced oxygen concentrations. The subscript N denotes LQ radiosensitivity parameters determined under normoxic ($>21\%$ O_2) conditions. Except when noted otherwise, measured data from published figures was digitized using the GetData Graph Digitizer© software. The analysis includes data for CHO cells (*32*, *51*, *52*), V79 cells (*33*, *49*, *53*, *55–57*), human kidney T-1 cells (*44*), and U251 human glioma cells (*54*) exposed to low-LET radiation (*33*, *44*, *49*, *51–57*) as well as cells exposed to particles with a range of LET (5.6–166 keV/um) (*32*, *36*, *43*) under normoxic and hypoxic conditions. Analyzed results from Spiro *et al.* (*56*), Ling *et al.* (*48*), Koch *et al.* (*47*), Gerweck *et al.* (*46*), and Michaels *et al.* (*50*) are also provided for cells irradiated by photons under oxygen concentrations ranging from anoxic to 100% O_2. For experiments that include multiple dose rates (*49*, *56*), the DSB repair half-time (τ) is treated as an adjustable parameter. Otherwise, a representative 2-h half-time for DSB repair is used to correct for dose protraction effects (*74*). The results of the extensive set of experiments for V79 and HSG cells irradiated with helium, carbon and neon ions reported by Furusawa *et al.* (*45*) were also reanalyzed. For the reanalysis, the estimates of α and β reported by Furusawa *et al.* (*45*) derived from independent fits to the data for normoxic and hypoxic cells were first used to generate synthetic data sets up to a surviving fraction of the order of 10^{-4}. The synthetic data sets were then refitted using the using the three-parameter (α_N, β_N and *HRF*) analysis method (*8*).

The induction and biological processing of DSBs is an important process underpinning the reproductive death of cells [(*7*) and references therein]. As a first approximation, the derivation of the LQ cell survival model from the RMF model suggests that α is proportional to the initial number of DSB Gy^{-1} cell^{-1}, and β is proportional to the square of the initial number of DSB Gy^{-1} cell^{-1}. For cells irradiated under reduced oxygen and then returned to a normoxic environment shortly thereafter, a temporary reduction in the available oxygen has a nominal impact on DSB repair kinetics (*8*). For the end point of clonogenic survival, HRF_α and HRF_β are thus related to the *HRF* for DSB induction by

TABLE 2
Summary of Published Cell Survival Data Sets Used to Determine MCDS Parameters Related to the Chemical Repair and Oxygen Fixation of the DNA Radicals Formed by Ionizing Radiation

Cell type	Radiation type	Energy (MeV/u)	Dose (Gy)	Dose rate (Gy/h)	$(Z_{eff}/\beta)^2$	$S - S_{\mathrm{rad}}$ (keV/μm)
CHO	X rays	200 kVp	1–18	294	18.8	1.53
	^{12}C	24	0.05–6	1800	725	80.0
CHO-AA8	γ rays	^{60}Co	2–5.9	348	1.72	0.24
CHO	X rays	270 kVp	0.4–3	18	14.1	1.30
			3.6–30.4	84		
V79-4	γ rays	^{60}Co	1.5–20.9	228	1.72	0.24
	^{4}He	0.83	0.5–4	1440	2095	119
V79	γ rays	^{137}Cs	9.9–100.9	0.89–276	2.8	0.34
	γ rays and X rays	^{60}Co and 10/15 MV	7.1–25.1	12–650	1.4–1.7	0.22−0.24
V79	X rays	200 kVp	1.2–11.9	72	18.9	1.60
V79–171	X rays	270 kVp	0.4–28	100	14.1	1.30
V79	X rays	10 MV	4–60	600	1.5	0.23
	γ rays	^{137}Cs	6.6–70.7	3.37	2.8	0.34
	γ rays	^{137}Cs	14–63.7	0.89	2.8	0.34
V79-379A	X rays	250 kVp	0.08–33	36.6	15.9	1.40
Hk–T1	X rays	250 kVp	1–22	120	15.9	1.40
	^{2}H	1.5, 7.45	1.4–19.9	40	63.7–617.5	5.7, 32.8
	^{4}He	0.63, 1.0	0.4–2.8	108	1770–2642	105, 140
	^{4}He	6.25, 2.08, 1.28	0.5–13	40	301–1412	26.3, 62, 88.6
V79-379A	X rays	250 kVp	1–20	96	15.9	1.40
	^{1}H	1.9, 1.15, 0.76	1–20	100	247.5–610	16.8, 24.4, 32.5
	^{4}He	0.95	1–6	1000	1854	109
CHO	X rays	50 kVp	3.7–26.2	120	25.7	2.13
	X rays	280 kVp	5–30	162	13.8	1.28
V79 S–171	γ rays	^{137}Cs	3–45.5	271	2.8	0.34
CHO	X rays	280 kVp	3–33	168	13.8	1.28
CHO	X rays	50 kVp	4.6–26.6	120	25.7	2.13
V79	^{3}He	10.1–1.27	0.5–31	32	188–1429	18.0–89.4
	^{12}C	82.3–1.92	0.5–27		231–7280	30.1–499
	^{20}Ne	130–7.71	0.5–21		435–5728	59.7–520
HSG	^{3}He	10.2–1.76	0.5–22		186–1050	17.8–70.6
	^{12}C	126–1.92	0.5–27		160–7280	22–499
	^{20}Ne	130–5.58	0.5–15		435–7546	60–645
U251	γ rays	^{60}Co	1–10	12	1.7	0.24
	X rays	8.04 keV	1.1–4.4		32.5	2.70

[a] a: aerobic; h: hypoxic.

$$HRF_{dsb}([O_2]) \cong HRF_{\alpha}([O_2]) = \frac{\alpha_N}{\alpha([O_2])}. \tag{10}$$

$$HRF_{dsb}([O_2]) \cong \sqrt{HRF_{\beta}([O_2])} = \sqrt{\frac{\beta_N}{\beta([O_2])}}. \tag{11}$$

3. *Estimation of MCDS parameters related to oxygen fixation and chemical repair*

The three-step algorithm to incorporate oxygen effects into the MCDS ultimately introduces four adjustable parameters into the modeling process, i.e., the parameters K, M_0, q and r determine the probability p_R an initial DNA radical formed by ionizing radiation undergoes chemical repair. Conceptually, p_R is closely related to the effects of oxygen on the formation of *individual* lesions within the DNA. As a first approximation, the *HRF* for the end points of single-strand break (SSB) and DSB induction are related to p_R by

$$HRF_{ssb} \cong \frac{1}{1 - p_R(x, [O_2])} \tag{12}$$

$$HRF_{dsb} \cong \left[\frac{1}{1 - p_R(x, [O_2])}\right]^2 \tag{13}$$

The rationale for Eq. (12) is that SSBs must be composed of at least one strand break. Hence, the chemical repair of a DNA radical with the potential to form a strand break will, as a first approximation, produce a corresponding reduction in the measured SSB yield detected using many experimental assays. Similarly, DSBs are composed of a minimum of two strand breaks on opposed DNA strands, and the chemical repair of the DNA radical precursor to either of the strand breaks forming a DSB will reduce the number of experimentally detected DSBs. As a test of the validity of Eqs. (12) and (13), MCDS cluster yields are compared to measured data from experimental assays for the detection of DSBs and other types of clusters. To the

TABLE 2
Extended

O_2 concentration[a]	Ref.
a: 95% air; h: -	(*32*)
a: 100% air; h: -	(*51*)
a: -; h: $< 0.0005\%$ O_2	(*52*)
a: 95% air; h: $< 0.0003\%$ O_2	(*33*)
a: 100% air; h: 0.001% O_2	(*49*)
a: - h: $< 0.0005\%$ O_2	(*53*)
a: 95% air; h: $< 0.0005\%$ O_2	(*55*)
21, 10, 3, 1, 0.3, 0.1, 0.03, 0.001% O_2	(*56*)
21, 10, 3, 1, 0.3, 0.1, 0.001% O_2	
21, 1, 0.3, 0.1, 0.03, 0.01, 0.001% O_2	
a: 95% air; h: $< 0.001\%$ O_2	(*57*)
a: 97% air; h: $< 0.005\%$ O_2	
	(*43*)
	(*44*)
a: 95% air; h: -	(*36*)
21, 10.5, 4, 1, 0.44, 0.21, 0.11, 0.05, $< 0.0005\%$ O_2	
100, 21, 0.44, 0.2, 0.11, $< 0.0005\%$ O_2	(*48*)
95, 1, 0.5, 0.1, < 0.0025, 2, 0.7, 0.4, 0.05, 0.02% O_2	
95, 19, 4, 1, 0.44, 0.2, 0.052, 0.002% O_2	(*47*)
21, 0.44, 0.21, $< 0.0005\%$ O_2	(*46*)
a: 100% air; h: -	(*50*)
a: 95% air; h: -	(*45*)
a: 100% air; h: -	(*54*)

extent that Eqs. (12) and (13) hold, substitution of Eq. (7) into the right-hand-side of Eqs. (12) and (13) gives

$$HRF_{ssb} \cong \sqrt{HRF_{dsb}} \cong \frac{[O_2] + M(x) \cdot K}{[O_2] + K} \tag{14}$$

DSB and Non-DSB (Fpg and Endo III) Clusters in HeLa Cells

New experimental assays for the detection of clustered DNA lesions other than the DSB provide additional opportunities to test the MCDS. One assay for the detection of non-DSB clusters is based on the postirradiation *in vitro* processing of isolated DNA by human or bacterial repair enzymes participating in the BER pathway, such as the *E. coli* Fpg protein (a DNA glycosylase) and Endonuclease III [reviewed in ref. (*22*)]. Postirradiation processing of DNA from irradiated cells with Fpg converts many types of oxidized purine (adenine and guanine) and some abasic sites into strand breaks. The postirradiation processing of DNA from irradiated cells with Endo III converts many types of oxidized pyrimidine (cytosine and thymine) and some abasic sites into strand breaks. Ultimately, the postirradiation processing of DNA by repair enzymes converts some non-DSB clusters into damage detectable as DSBs with the neutral (non-denaturing) gel electrophoresis assay. That is, fragment size distributions from constant- or pulsed-field gel electrophoresis are quantified and then converted to estimates of the number of DSBs per cell (or per Gbp) using number average length analysis (NALA) with and without application of the repair enzymes. Numbers of Fpg and Endo III clusters are determined by subtracting the number of DSBs formed directly by radiation (i.e., without application of the repair enzymes) from the total number of DSBs obtained with the application of repair enzymes (*22*).

1. Measurement of DSB and non-DSB cluster using the PFGE assay

We measured DSB and non-DSB clusters in HeLa cervical carcinoma cells for normoxic (21% O_2) and reduced oxygen ($O_2 <$ 0.2%) conditions using the pulsed-field gel electrophoresis (PFGE) assay. Preparation of human DNA in agarose plugs was performed as described in ref. (*6*). Briefly, approximately 250,000 cells were embedded in low-melting-point agarose plugs and, after lysis at neutral conditions, plugs were acclimated extensively in the appropriate enzyme buffer and treated with *E. coli* enzymatic damage probes (Fpg, Endo III) for the detection of Fpg (oxypurine) or Endo III (oxypyrimidine) clusters. After enzyme treatment, samples were incubated in a proteinase K-based reaction stop buffer and then neutralized in 0.5× TBE running buffer. For the measurement of DSB and non-DSB clusters, samples and molecular length standards were electrophoresed in a 0.85% neutral agarose gel (Bio-Rad Megabase Agarose, (Bio-Rad, Hercules, CA) prepared in 0.5× TBE) in a BioRad CHEF (contour-clamped homogeneous electric field) DR-II apparatus (field angle 120°) with a dual switch time of 40–3600 s for 82 h at 2 V/cm and then 5–40 s for 6 h at 5 V/cm at 12°C. Gels were stained with ethidium bromide (1 μg/ml in double distilled water) for 1 h and destained overnight, and an electronic image was obtained using a FluorChem™ 8800 imaging system (Alpha Innotech, San Leandro, CA). Electronic images were then processed using QuantiScan (BioSoft, Cambridge, UK) to obtain a densitogram for each gel lane. The analysis of the gels was performed using number average length analysis (NALA). DSB yields and non-DSB clusters were calculated for each case (*23*).

Experiments under reduced oxygen conditions ($<$21% O_2) are performed using the thin-film method for rapid gas-liquid equilibration (*75*) to establish a hypoxic environment prior to irradiation of cell cultures. Glass dishes coated with collagen were kept at 37°C without CO_2 for 18 h. Then conditioned medium was aspirated and replaced with 1 ml 0.2% gelatin for 1 h. Medium and gelatin were aspirated and the plates sterilized with UV radiation for 20 min. Then 2 ml of medium containing full DMEM was added and equilibrated in the incubator for 2 h. Approximately 10^6 cells were seeded per plate and left to attach overnight. Prior to irradiation, cells were exposed to a specified percentage of O_2 using a series of precision chamber evacuations followed by replacement with nitrogen gas exchanges. After warming, the chambers were shaken continuously at 37°C to ensure that the O_2 in the gas phase was in equilibrium with the O_2 in the culture medium. After exposure to hypoxia for 30 min, the aluminum chambers were placed directly in the ^{137}Cs irradiator (dose rate ~2 Gy per minute). Irradiated and sham-irradiated cells were harvested at various times 0 to 48 h postirradiation and centrifuged at 1,000 rpm. Cell pellets were snap frozen in ethanol/dry ice bath and prepared for DNA damage analysis.

2. Cell-specific Monte Carlo simulations of DSB and non-DSB clusters

Although explicit Monte Carlo simulation of the induction and subsequent processing of initial base damage by the Fpg and Endo III enzymes is presently beyond the scope of the MCDS, comparisons of the different categories of individual or clustered base damage may still provide useful clues as to the identity or complexity of the damage detected in experimental assays as Fpg or Endo III clusters. Because

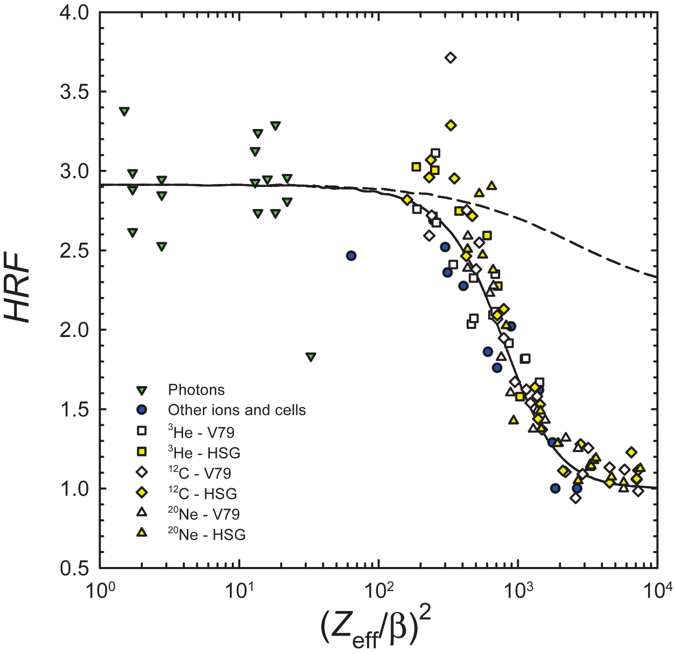

FIG. 1. Comparison of the *HRF* for clonogenic survival to the *HRF* for DSB induction. Filled and open symbols denote estimates of the *HRF* for clonogenic cell survival derived from published experiments (Table 2) for cells under extreme hypoxia ($<0.01\%$ O_2). Solid line: *HRF* for DSB induction predicted by the MCDS ($M_0 = 1.740$, $K = 0.3372\%$ O_2, $q = 946.1$, $r = 2.150$). Dashed line: *HRF* for DSB induction predicted by the MCDS when $M(x)$ approaches the asymptotic value $M_0 = 1.740$ as $q \rightarrow \infty$. For this special case, the probability an initial DNA radicals undergo chemical repair instead of fixation is the same for all ions, regardless of radiation quality.

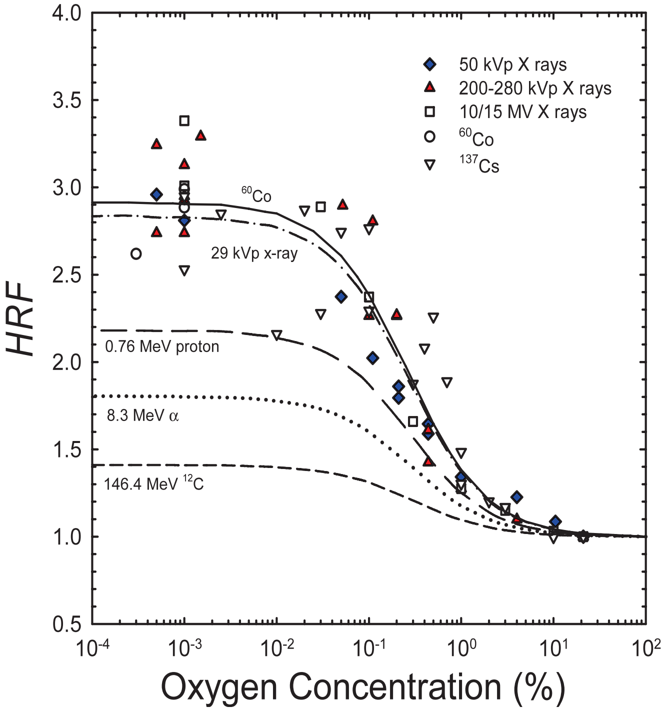

FIG. 2. Effects of oxygen concentration on the *HRF* for clonogenic cell survival and DSB induction. Symbols: *HRF* for clonogenic survival derived from published cell survival experiments for photons (Table 2). Lines denote the *HRF* for DSB induction predicted by the MCDS for ^{60}Co (solid line), 29 kVp X rays with 30-μm Mo filter (dash dot line), 0.76 MeV protons (long dashed line), 8.3 MeV α particles (dotted line), and 146.4 MeV carbon ions (short dashed line).

DSB formation requires at least two strand breaks on opposite sides of the DNA double helix within about 10 bp of each other, the postirradiation application of Fpg and Endo III has the potential to convert a strand break with base damage (or an abasic site) in the opposed strand to a DSB. Clusters with base damage on opposed strands may also be converted to a DSB. As a working hypothesis, any non-DSB cluster composed of two or more lesions with at least one lesion on opposing sides of the DNA helix may be converted to a DSB through postirradiation application of Fpg and Endo III. The MCDS provides information about the relative numbers of SSBs and clustered base damage composed of exactly *k* lesions (e.g., *k* = 1, 2, 3, ...). To relate the MCDS estimates of the initial numbers of non-DSB clusters to the number of Fpg and Endo III clusters, we propose the following formulas:

$$\sigma_{Fpg}([O_2]) = \kappa_{HeLa} f_{Fpg} \sigma_k([O_2]). \tag{15}$$

$$\sigma_{Endo\,III}([O_2]) = \kappa_{HeLa} f_{Endo\,III} \sigma_k([O_2]). \tag{16}$$

Here, κ_{HeLa} is a dimensionless factor that corrects for cell-specific biology impacting equally on all types of individual or clustered DNA lesions (e.g., the DNA content per cell), and $\sigma_k([O_2])$ is the initial number of non-DSB clusters with exactly *k* lesions produced in a cell irradiated under oxygen concentration $[O_2]$. We assume that fraction f_i of the initial σ_k clusters (*i* = Fpg or Endo III) are converted to a DSB through the postirradiation action of the Fpg and Endo III enzymes. To minimize the number of adjustable parameters and probe the relationship between different categories of non-DSB cluster, the MCDS is used to estimate σ_k as a function of O_2 concentration. The parameters κ_{HeLa}, f_{Fpg} and $f_{Endo\,III}$ are considered cell- and assay-specific adjustable parameters that are independent of the O_2 concentration at the time of irradiation.

RESULTS AND DISCUSSION

Comparisons of HRF for Cell Survival and DSB Induction

To estimate the four key input parameters (M_0, *K*, *q*, *r*) needed to model the effects of chemical repair and oxygen fixation within the MCDS, we performed a non-linear regression analysis of published cell survival data (Table 2) to estimate the *HRF* as a function of oxygen concentration and radiation quality using Eqs. (10) and (11) (symbols in Figs. 1 and 2). To estimate MCDS inputs related to oxygen fixation and chemical repair, a second non-linear regression analysis was performed to minimize a positively weighted sum of the difference between the *HRF* computed using Eq. (13) and the *HRF* derived from the clonogenic survival data (i.e., the sum of squared error). Because the *HRF* for DSB induction computed using Eq. (13) is an approximation, we manually fine-tuned the estimates of M_0, *K*, *q* and *r* to minimize the difference between the Monte Carlo-simulated *HRF* for DSB induction [i.e., Eq. (9)] and the *HRF* derived from the cell survival data [Eqs. (10) and (11)]. Other MCDS input parameters related to the simulation of DNA damage under normoxic conditions were maintained the

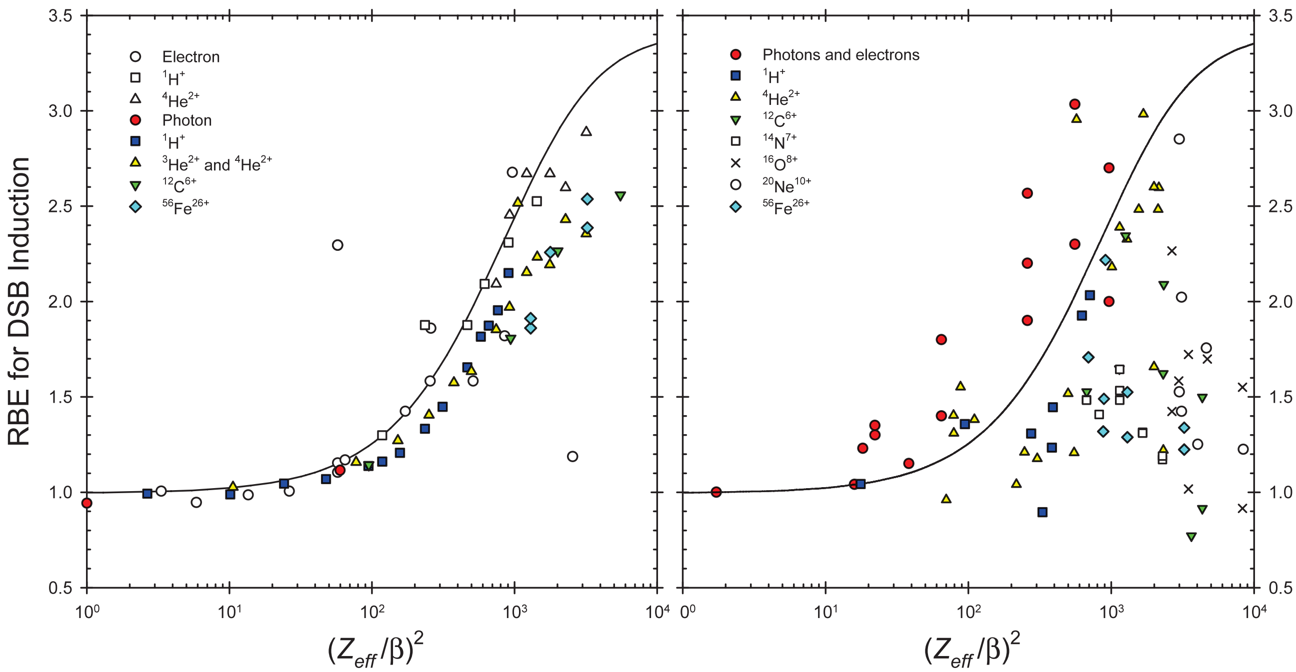

FIG. 3. Effects of radiation quality on DSB induction in well oxygenated cells. Solid lines: RBE for DSB induction predicted by the MCDS with ^{60}Co as the reference radiation. Symbols: RBE for DSB induction from published track structure simulations (left panel) and pulsed-field gel electrophoresis (PFGE) measurements (right panel). Left panel: open symbols (*85–89*) and filled symbols (*78*, *90*). Right panel: photons and electrons (*31*, *33*, *80*, *91–95*), protons (*15*, *96–103*), α particles (*15*, *31*, *94*, *96–102*), ^{12}C (*97*, *99*, *103*), ^{14}N (*80*, *101*, *104–105*), ^{16}O (*97*, *103*), ^{20}Ne (*97*, *99*, *103*), and ^{56}Fe (*6*, *79–80*, *106–108*). For published studies that did not report DSB yields for ^{60}Co γ rays, estimates of RBE with ^{60}Co as the reference radiation were computed as $\text{RBE}_X \times \text{RBE}_{60}$. Here, RBE_X is the RBE of the radiation of interest relative to reference radiation X, and RBE_{60} is the RBE of reference radiation X relative to ^{60}Co γ rays. Estimates of RBE_{60} derived from MCDS simulations ranged from 1.005 to 1.3 for results from Nikjoo *et al.* (*85–89*) and were <1.05 for data from all other publications.

same as in our previous publication (*13*). The oxygen effect parameters selected as optimal from this multistep analysis were: $M_0 = 1.740$, $K = 0.3372\%$ O$_2$, $q = 946.1$, $r = 2.150$.

Figure 1 shows a comparison of the *HRF* for clonogenic survival derived from published experiments (Table 2) to the *HRF* for DSB induction predicted by the MCDS with the best-fit parameters (solid line: $M_0 = 1.740$, $K = 0.3372\%$ O$_2$, $q = 946.1$, $r = 2.150$) and for the special case when $q \rightarrow \infty$ (dashed line). The MCDS-predicted *HRF* for DSB induction is ~2.9 for particles with $(Z_{eff}/\beta)^2$ less than ~100. As $(Z_{eff}/\beta)^2$ increases, the *HRF* decreases in a monotonic fashion and approaches unity for radiations with $(Z_{eff}/\beta)^2$ greater than ~4000. An *HRF* equal to unity means that the ion produces the same DSB yield under normoxic and hypoxic conditions. For the special case when $q \rightarrow \infty$, the function $M(x)$ approaches the asymptotic value of M_0, regardless of particle type and energy [refer to Eq. (8)]. Conceptually, this special case corresponds to a scenario in which the probability that the initial DNA radical undergoes chemical repair instead of fixation is the same for all ions, regardless of radiation quality. When $q \rightarrow \infty$ (Fig. 1, dashed line), the *HRF* for ions with $(Z_{eff}/\beta)^2$ greater than about 100 is larger than the *HRF* derived from the measured data (Fig. 1, symbols). This observation suggests that the chemical repair process becomes less effective, per initial DNA radical, as $(Z_{eff}/\beta)^2$ (and hence particle LET) increases.

A possible explanation for the inferred decrease in the effectiveness of the chemical repair process is clustering of initial DNA radicals on a single nucleotide because of the dense patterns of ionization and excitations associated with high-LET radiations. As a conceptual example, imagine that densely ionizing radiation creates multiple radicals in close enough spatial proximity to a single nucleotide (sugar, base or phosphate group) that the nucleotide is ultimately converted to a strand break unless all of the initial radicals are reduced. In this scenario, the chemical restoration of a subset of the radicals formed on a nucleotide would be ineffective at preventing the formation of a strand break – in effect, the chemical repair process becomes less effective per initial DNA radical. Regardless of the underlying mechanism, the *HRF* for DSB induction predicted by the MCDS with the proposed model and selected input parameters (Fig. 1, solid line) captures well the overall trends in the *HRF* derived from clonogenic survival for a wide range of particle types and energies, including the *HRF* for the proton and carbon ions of interest in radiation therapy (*76*, *77*).

Figure 2 shows, for a range of oxygen concentrations, a comparison of the *HRF* for clonogenic survival to the *HRF* for DSB induction predicted by the MCDS. For photons and other radiations with a low $(Z_{eff}/\beta)^2$, the predicted *HRF* is close to the maximum of 2.9 for oxygen concentrations less

TABLE 3
Comparison of Measured and Predicted Estimates of HRF_{dsb} for Selected Cell Lines and Types of Ionizing Radiation

Experimental technique	Cell type	Radiation type	Energy (MeV/u)	$(Z_{eff}/\beta)^2$	$S - S_{rad}$ (keV/μm)	Dose (Gy)
SFGE cold lysis	CHO	X rays	200 kVp	18.8	1.53	0–125 0–400
		^{12}C	24	725	80	0–60 0–180
Sucrose sedimentation	V79-4	γ rays	^{60}Co	1.72	0.24	0–250 60–150
		^{4}He	0.83	2095	119	0–200 100–200
Neutral filter elution	VH10 normal human fibroblasts	γ rays	^{137}Cs	2.80	0.34	0–50 10–50
Neutral filter elution	V79-379A	X rays	250 kVp	15.9	1.4	– –
		X rays	1.487 keV	173	8.3	2.5–20 2–40
Neutral filter elution	V79-379A	^{1}H	1.15	407	24	20–50 2–40
		^{1}H	0.76	610	31	20–50 20–50
		^{4}He	0.95	1854	107	20–50 20–50
PFGE warm lysis	RT112 human bladder carcinoma	γ rays	^{60}Co	1.72	0.24	20–200 50–350
Sucrose sedimentation	rad 52 (PR 94)	e^-	30 MeV	1.00	0.21	300–2400 200–1500
		^{4}He	0.875	1994	113	100–350 100–400
PFGE cold lysis	V79-4	γ rays	^{60}Co	1.72	0.24	5–20 –
		X rays	4.55 keV	64.6	4.4	5–19 –
			1.49 keV	259	10.3	– –
			0.96 keV	556	15	– –
			0.28 keV	965	18	2–7 –
Neutral PFGE lysis at 37°C						
	HeLa	γ rays	^{137}Cs	2.80	0.34	5

[a] a: aerobic, h: hypoxic.

[b] For MCDS simulations, aerobic and hypoxic O_2 concentrations not specified in the reference are taken as 21% and 10^{-3}%, respectively.

[c] Reported DSB yields are 2.7 and 0.7 DSB Gy^{-1} Gbp^{-1} for aerobic and hypoxic conditions, respectively.

than 0.01%. The photon *HRF* decreases rapidly in a monotonic fashion toward unity as oxygen concentration increases. The *HRF* for DSB induction predicted by the MCDS (Fig. 2, solid line) is in good agreement with the *HRF* derived from the survival data for cells irradiated by photons under a wide range of oxygen conditions. For cells irradiated under conditions comparable to the oxygen concentrations typically found in normal tissue (i.e., 5–8% O_2), the predicted *HRF* ranges from 1.06 to 1.09. Also shown in Fig. 2 is the predicted effect of oxygen concentration on the *HRF* for DSB induction by selected ions (0.76 MeV protons, 8.3 MeV α particles, and 146.4 MeV ^{12}C ions). Regardless of the type of ion, the predicted *HRF* for DSB induction approaches unity for oxygen concentrations beyond about 10%. However, the RBE of higher-LET radiations compared to ^{60}Co γ rays tends to *increase* with *decreasing* oxygen concentration. The predicted RBE for DSB induction of a 1 MeV proton (26.9 keV/μm) relative to ^{60}Co γ rays (0.24 keV/μm) increases from 1.9 to 2.3 as the oxygen concentration decreases from 100% to 0%. For a 12 MeV ^{12}C ion (681 keV/μm), the predicted RBE for DSB induction increases

TABLE 3
Extended

		MCDS[b]		
O_2 concentration[a]	Reported HRF_{dsb}	DSBs Gy^{-1} Gbp^{-1}	HRF_{dsb}	Ref.
a: 95% air	3.4	8.5	2.85	(*32*)
h: -		3.0		
a: 95% air	2.2	18.2	1.99	
h: -		9.1		
a: 95% air	5	8.1	2.86	(*33*)
h: < 0.0003% O_2		2.8		
a: 95% air	1.2	24.1	1.19	
h: < 0.0003% O_2		20.3		
a: 100% air	2.6	8.1	2.85	(*34*)
h: < 0.0005% O_2		2.9		
a: 95% air	3.5	8.4	2.85	(*35*)
h: < 0.0006% O_2		3.0		
a: 95% air	1.64	11.7	2.79	
h: < 0.0006% O_2		4.2		
a: 95% air	1.64	14.9	2.46	(*36*)
h: -		6.1		
a: 95% air	1.49	17.1	2.15	
h: -		8.0		
a: 95% air	1.14	23.5	1.24	
h: -		19.0		
a: 3% O_2	3.86[b]	7.2	2.54	(*37*)
h: < 0.001% O_2		2.8		
a: 100% air	2.80	8.3	2.90	(*31*)
h: -		2.8		
a: 100% air	1.30	23.8	1.20	
h: -		19.8		
a: 95% air	3.50	8.3	2.92	(*91*)
h: -		2.8		
a: 95% air	1.90	9.7	2.89	
h: -		3.4		
a: 95% air	2.10	13.1	2.70	
h: -		4.9		
a: 95% air	1.80	16.8	2.27	
h: -		7.4		
a: 95% air	1.80	20.0	1.73	
h: -		11.6		
a: 21% O_2	1.00	8.15	1.00	This work
a: 1% O_2	1.08	6.00	1.36	
a: 0.5% O_2	1.27	5.03	1.62	
a: 0.1% O_2	1.90	3.47	2.35	
h: -	1.90	2.84	2.87	

from 3.4 (100% O_2) to 9.8 (0% O_2). As illustrated in Fig. 1, the *HRF* for DSB induction predicted by the MCDS for protons and more massive ions is in good agreement with the *HRF* for clonogenic cell survival under extreme hypoxia (<0.01%).

Comparisons of RBE and the HRF for DSB Induction

Figure 3 compares MCDS estimates (solid lines) of the RBE for DSB induction to estimates from track structure simulations (left panel) and from PFGE measurements (right panel) under normoxic conditions. The MCDS predicts that the RBE for DSB induction increases rapidly up to a $(Z_{eff}/\beta)^2$ of about 4,000 and then increases in a more gradual, monotonic fashion up to $(Z_{eff}/\beta)^2 = 10{,}000$. The MCDS-predicted trends in RBE are quite similar to the ones predicted by detailed track structure simulations (*78*, *79*) for ions up to and including ^{56}Fe, although the absolute numbers of DSBs and the RBE may differ by as much as 30% for some high-LET radiations. However, the differences in RBE estimates among the track structure simulations from different groups are about as large as the differences between the MCDS estimates and the estimates from either group's track structure simulations (Fig. 3, left panel). In comparison to the reasonable agreement among results from the MCDS and track structure simulations, measured estimates of the RBE for DSB induction appear to increase with increasing $(Z_{eff}/\beta)^2$ up to about 1000 and then start to decrease (Fig. 3, right panel).

The seeming discrepancies among the measured and predicted RBE estimates for large $(Z_{eff}/\beta)^2$ are reasonably attributed to the challenges associated with measuring small DNA fragments using the PFGE assay (*78*, *80*). That is, massive particles with a large LET are much more effective at producing spatially correlated DSBs in the same chromosome than lower-LET radiations. The small DNA fragments produced by pairs of DSBs in close spatial proximity often go undetected in the PFGE assay; hence the measured DSB yield is underestimated for heavier ions but not for electrons and photons. In contrast to the discrepancies among the measured and predicted RBE estimates for massive ions, the measured and predicted RBE estimates are in reasonable agreement for low-energy (high-LET) photons (red filled circles in the right panel of Fig. 3). This observation is consistent with the hypothesis that uniform irradiation of a cell by large numbers of low-energy photons produces spatially dispersed (uncorrelated) DSBs rather than spatially correlated DSB.

Table 3 compares the MCDS-predicted *HRF* for DSB induction to estimates derived from measured data. The MCDS and measured estimates of the *HRF* for DSB induction decrease with increasing $(Z_{eff}/\beta)^2$. The trends in the *HRF* derived from direct measurements of the DSB yield with radiation quality are consistent with the trends and the absolute magnitude of the *HRF* derived from clonogenic survival data (Fig. 1). The reported *HRF* values for different types of low-LET radiation vary greatly among the published experiments. The differences among the measured estimates of the *HRF* provide some evidence that the presence or absence of oxygen at the time of irradiation has an impact on the initial induction of DNA damage in ways that are cell line and cell type specific. However, the variability in the measured *HRF* may also be a reflection of known artifacts and uncertainties associated with the experimental detection of DSBs using various techniques (*16*, *78*, *81*, *82*). Although the MCDS includes an option to scale absolute cluster yields for cell DNA content, other cell-specific biological factors (e.g., chromatin structure) are

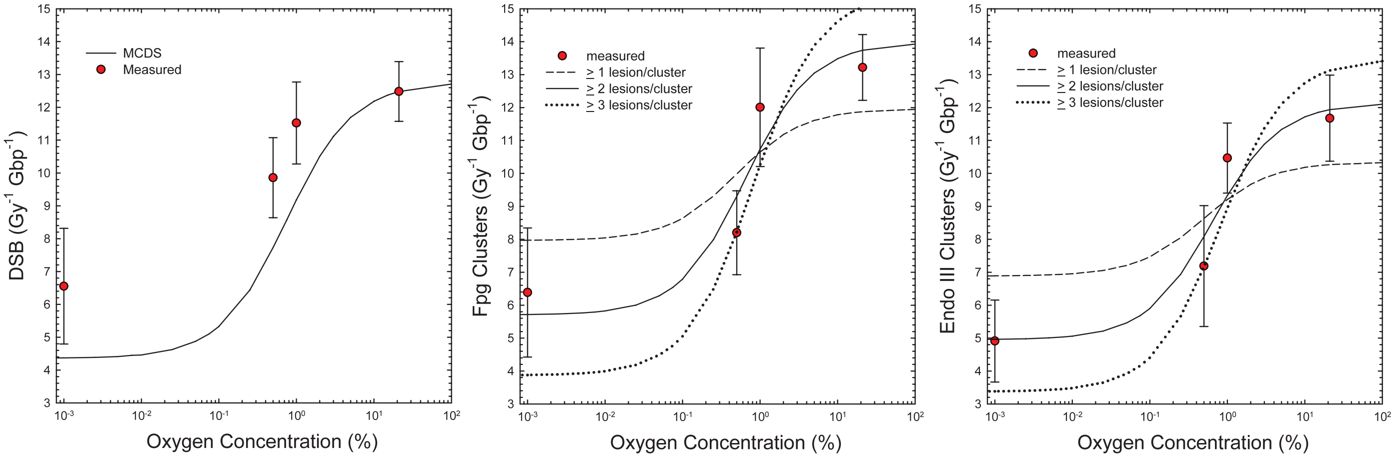

FIG. 4. Effects of oxygen on the induction of DSB and non-DSB (Fpg and Endo III) clusters in HeLa cells exposed to 5 Gy of γ rays from ^{137}Cs. Symbols: measured data from PFGE assay. Solid line (left panel): MCDS estimates of the DSB yield normalized to reproduce the measured yield at 21% O_2. Solid lines (center and right panels): fraction *f* of the initial non-DSB clusters composed of 2 or more lesions ($k = 2$) converted to DSBs by the Fpg glycosylase ($f_{Fpg} = 0.055$) or the Endo III nuclease ($f_{Endo\ III} = 0.048$). Dashed lines (center and right panels): fraction *f* of the initial non-DSB clusters composed of 1 or more lesions ($k = 1$) converted to a DSB by Fpg ($f_{Fpg} = 0.013$) or Endo III ($f_{Endo\ III} = 0.011$). Dotted lines (center and right panels): fraction *f* of the initial non-DSB clusters composed of 3 or more lesions ($k = 3$) converted to a DSB by Fpg ($f_{Fpg} = 0.23$) or Endo III ($f_{Endo\ III} = 0.20$). All MCDS results are scaled by $\kappa_{HeLa} = 1.53$ to correct for cell-specific biology not explicitly considered in the Monte Carlo model. For visualization purposes, measured data for 0% (nominal) O_2 are shown at the 0.1% O_2 level.

not explicitly considered in the MCDS. To simulate the absolute numbers of clusters produced in a specific experimental system, one or more of the default (recommended) biological inputs to the MCDS may need to be adjusted to better reflect the characteristics of a particular cell line, cell type or environment (e.g., confluent or rapidly dividing cells). Still, we consider the overall trends in the RBE and *HRF* for DSB induction to be in good agreement with measured data for a wide range of particle types, energies and oxygen concentrations.

Comparison of Absolute Numbers of DSB and non-DSB Clusters

In our experiments, we detected 12.48 DSBs Gy^{-1} Gbp^{-1} in HeLa cervical carcinoma cells irradiated by γ rays from a ^{137}Cs source compared to the MCDS estimate of 8.16 DSBs Gy^{-1} Gbp^{-1} for a representative mammalian cell irradiated under 21% O_2 by ^{137}Cs γ rays. The cell-specific correction factor κ_{HeLa} is approximately equal to 12.48 DSBs Gy^{-1} Gbp^{-1}/8.16 DSBs Gy^{-1} Gbp^{-1} = 1.53. To fit Eqs. (15) and (16) to the measured yields of Fpg and Endo III clusters, the enzyme-specific factors f_{Fpg} and $f_{Endo\ III}$ were adjusted to minimize a positively weighted sum of the squared errors between the measured and calculated yields of Fpg and Endo III clusters. The model for Fpg and Endo III clusters was fitted to the measured data for several different categories of non-DSB cluster, including all non-DSB clusters composed of 1 or more lesion, all non-DSB clusters composed of 2 or more lesions, and all non-DSB clusters composed of 3 or more lesions. We also fitted the model to the measured cluster yields for different categories of non-DSB clusters (i.e., SSBs and clusters composed solely of base damage).

Of the categories considered, non-DSB clusters composed of two or more lesions ($k = 2$) best minimize differences among the measured and predicted yields of Fpg and Endo III clusters (solid lines in Fig. 4). As shown in Fig. 4 (dashed and dotted lines; center and right panels), trends in the predicted number of Fpg and Endo III clusters (Gbp^{-1} Gy^{-1}) with O_2 concentration for $k = 1$ (all non-DSB clusters composed of one or more lesions) and $k = 3$ (all non-DSB clusters composed of 3 or more lesions) are substantially over- or underpredicting cluster yields for some O_2 concentrations. The model predicts that about 5.5% of the non-DSB clusters composed of 2 or more lesions are converted to Fpg clusters ($f_{Fpg} = 0.055$) and about 4.8% of the non-DSB clusters composed of 2 or more lesions are converted to Endo III clusters ($f_{Endo\ III} = 0.048$). The MCDS predicts that the number of non-DSB clusters composed of 2 or more lesions comprise 27% of the total non-DSB clusters at 21% O_2 and 17% of the total non-DSB clusters at 0.1% O_2. The good agreement between the measured and predicted Fpg and Endo III cluster yields for the non-DSB clusters composed of 2 or more lesions (Fig. 4, solid line), but not clusters composed of 1 or more or 3 or more (Fig. 4, dashed and dotted lines), suggests that substantial numbers of non-DSB clusters composed of 2 lesions are converted to DSBs through the postirradiation application of the Fpg and Endo III enzymes. The good agreement in terms of the absolute numbers of DSB, Fpg and Endo III clusters shown in Fig. 4 also provides evidence that the effects of oxygen on clustered DNA lesions are adequately modeled in the MCDS.

SUMMARY AND CONCLUSIONS

Prior publications (*13*, *58*) provide evidence that the MCDS is capable of estimating the overall yield of SSBs, DSBs and clustered base damage produced in a normal, well-oxygenated cellular environment by electrons, protons and α particles with energies as high as 1 GeV. In this work, comparisons of MCDS estimates of RBE and the *HRF* to data from other published experimental and theoretical studies provide evidence suggesting that the MCDS captures the major trends in the production of DSBs and non-DSB clusters for ions up to and including ^{56}Fe. The MCDS has been extended so that the induction of individual and clustered DNA lesions can be simulated for arbitrary mixtures of different types of radiation in cells irradiated in hypoxic and aerobic environments. For radiations with $(Z_{eff}/\beta)^2$ less than 100, the predicted hypoxia reduction factor (*HRF*) for DSB induction under anoxic conditions is 2.91, and the predicted *HRF* for SSB induction under anoxic conditions is 1.63. The Monte Carlo-predicted *HRF* for SSB induction is slightly smaller than the square root of the *HRF* for DSB induction (i.e., 1.7) because DSBs arise, on average, from larger numbers of lesions (or DNA radicals) than SSBs. Because the Monte Carlo simulation assumes that all of the initial DNA radicals formed by ionizing radiation are equally likely to be removed through the chemical repair process, the chemical repair of initial DNA radicals is slightly more effective, on average, at removing potential SSBs from the DNA than potential DSBs. As $(Z_{eff}/\beta)^2$ increases, the *HRF* decreases monotonically and approaches unity for $(Z_{eff}/\beta)^2$ greater than about 4,000. For all oxygen concentrations and types of ions, the predicted *HRF* for SSB induction is approximately equal to the square root of the *HRF* for DSB induction. Although additional comparisons of measured and predicted cluster yields are needed to more fully validate the MCDS, the reported studies provide evidence that plausible nucleotide-level maps of the clustered DNA lesions formed in cells irradiated under conditions of reduced oxygen by low- and high-LET radiation can be generated. Monte Carlo simulations of the induction of clustered DNA lesions by ionizing radiation are currently the only way to obtain nucleotide-level maps of the spatial configuration of the DNA lesions forming a cluster.

The MCDS algorithm to simulate the effects of oxygen on clustered DNA lesions is based on the widely held hypothesis that the effects of oxygen on individual and clustered DNA lesions arise from kinetic competition between the oxygen fixation and chemical repair processes. The reported studies suggest that the proposed algorithm, as implemented within the MCDS, is adequate to predict changes in the initial yields of DSBs as well as two types of non-DSB clusters, i.e., Fpg and Endo III clusters. The good agreement among biological indicators of radiation quality (RBE) and oxygen effects (*HRF*) derived from cell survival data and from direct measurements of the DSB yield also provides evidence supporting the widely held view that DSBs are a biologically critical form of clustered DNA lesion. However, the induction of Fpg and Endo III clusters exhibits similar trends with oxygen concentration, and the possibility that some types of non-DSB clusters play an important role in reproductive death cannot be easily dismissed. Experiments have shown that unsuccessful excision repair of non-DSB clusters *in vitro* and *in vivo* sometimes produces enzymatic DSBs [(*83*, *84*) and references therein] minutes or hours after cells are irradiated. Additional research is needed to investigate the potential significance of non-DSB clusters for radiation mutagenesis, cell death, neoplastic transformation and other end points related to carcinogenesis and the treatment of cancer using ionizing radiation.

Comparing dimensionless metrics of radiation quality (RBE) and oxygen concentration (*HRF*) for different end points is an especially useful way to test biological hypotheses linking early (*initial*) chemical alterations in biological targets to higher-level cellular or tissue end points. The quantity and complexity of initial damage to small biological targets are closely related to the predictable spatial features of energy deposits from individual ion tracks (i.e., track structure) whereas cell and tissue responses to radiation occur over much larger time and spatial scales and often arise from the combined effects of many ion tracks. At the multicellular and tissue levels, the deposition of energy may appear uniform (i.e., a uniform absorbed dose) even though the structure of the individual tracks is quite different. For a uniform absorbed dose, any difference in the response of a cell or tissue to one type of radiation relative to another type of radiation (*same dose*) must be attributed to differences in track structure or to the numbers of tracks required to deliver the dose. Dimensionless biological metrics, such as the RBE and *HRF*, help isolate the effects of radiation quality (*track structure*) and local oxygen concentration from the effects of other biological events and processes, such as intercellular signaling, cell-matrix interactions and inflammatory responses. A strong, positive correlation between the RBE and *HRF* for one end point (e.g., induction of DSBs or non-DSB clusters) with the RBE and *HRF* for a different end point (e.g., reproductive cell death or tumor control) is strong, albeit indirect, evidence that the mechanisms underlying both end points are causally linked. The MCDS captures many of the essential trends in the formation of DSBs and non-DSB clusters with radiation quality and oxygen concentration and is a useful tool to probe the multiscale effects and interactions of ionizing radiation in cells and tissues.

ACKNOWLEDGMENTS

The authors thank Dr. Vladimir A. Semenenko for developing the original MCDS algorithm and software and for providing useful feedback and suggestions on the current manuscript. The authors also thank Mr. Anshuman Panda for implementing an early version of the model for chemical repair and oxygen fixation. Work supported in part by American Cancer Society grant IRG-58-012-52 (DJC) and in part by a Research Creative Activity Grant from the East Carolina University (ECU) Biology Department (AGG). VKY and RDS contributed equally to the project. AGG and CK are responsible for measurements of DSB, Fpg and Endo III cluster yields in HeLa cells. VKY, RDG and DJC contributed to the collection, analysis and interpretation of data. JHP performed MCNP simulations of secondary electron energy spectra for photons. RDS is responsible for the overall conception and design of the project. All authors contributed to preparation of the manuscript.

Received: April 27, 2011; accepted July 4, 2011; published online: August 8, 2011

REFERENCES

1. Goodhead DT. Initial events in the cellular effects of ionizing radiations: clustered damage in DNA. Int J Radiat Biol 1994; 65:7–17.
2. Hlatky L, Sachs RK, Vazquez M, Cornforth MN. Radiation-induced chromosome aberrations: insights gained from biophysical modeling. Bioessays 2002; 24:714–23.
3. Ward JF. DNA damage produced by ionizing radiation in mammalian cells: identities, mechanisms of formation, and reparability. Prog Nucleic Acid Res Mol Biol 1988; 35:95–125.
4. Ward JF. Radiation mutagenesis: the initial DNA lesions responsible. Radiat Res 1995; 142:362–8.
5. Shikazono N, Noguchi M, Fujii K, Urushibara A, Yokoya A. The yield, processing, and biological consequences of clustered DNA damage induced by ionizing radiation. J Radiat Res (Tokyo) 2009; 50:27–36.
6. Tsao D, Kalogerinis P, Tabrizi I, Dingfelder M, Stewart RD, Georgakilas AG. Induction and processing of oxidative clustered DNA lesions in ^{56}Fe-ion-irradiated human monocytes. Radiat Res 2007; 168:87–97.
7. Carlson DJ, Stewart RD, Semenenko VA, Sandison GA. Combined use of Monte Carlo DNA damage simulations and deterministic repair models to examine putative mechanisms of cell killing. Radiat Res 2008; 169:447–59.
8. Carlson DJ, Stewart RD, Semenenko VA. Effects of oxygen on intrinsic radiation sensitivity: A test of the relationship between aerobic and hypoxic linear-quadratic (LQ) model parameters. Med Phys 2006; 33:3105–15.
9. Frese MC, Wilkens JJ, Huber PE, Jensen AD, Oelfke U, Taheri-Kadkhoda Z. Application of constant vs. variable relative biological effectiveness in treatment planning of intensity-modulated proton therapy. Int J Radiat Oncol Biol Phys 2011; 79:80–8.
10. Maucort-Boulch D, Baron MH, Pommier P, Weber DC, Mizoe JE, Rochat J, et al. Rationale for carbon ion therapy in high-grade glioma based on a review and a meta-analysis of neutron beam trials. Cancer Radiother 2010; 14:34–41.
11. Brizel DM, Sibley GS, Prosnitz LR, Scher RL, Dewhirst MW. Tumor hypoxia adversely affects the prognosis of carcinoma of the head and neck. Int J Radiat Oncol Biol Phys 1997; 38:285–9.
12. Roots R, Okada S. Estimation of life times and diffusion distances of radicals involved in x-ray-induced DNA strand breaks of killing of mammalian cells. Radiat Res 1975; 64:306–20.
13. Semenenko VA, Stewart RD. Fast Monte Carlo simulation of DNA damage formed by electrons and light ions. Phys Med Biol 2006; 51:1693–706.
14. Rothkamm K, Lobrich M. Evidence for a lack of DNA double-strand break repair in human cells exposed to very low x-ray doses. Proc Natl Acad Sci U S A 2003; 100:5057–62.
15. Frankenberg D, Brede HJ, Schrewe UJ, Steinmetz C, Frankenberg-Schwager M, Kasten G, et al. Induction of DNA double-strand breaks by ^{1}H and ^{4}He ions in primary human skin fibroblasts in the LET range of 8 to 124 keV/μm. Radiat Res 1999; 151:540–9.
16. Prise KM, Ahnstrom G, Belli M, Carlsson J, Frankenberg D, Kiefer J, et al. A review of dsb induction data for varying quality radiations. Int J Radiat Biol 1998; 74:173–84.
17. Frankenberg-Schwager M, Frankenberg D, Blocher D, Adamczyk C. The influence of oxygen on the survival and yield of DNA double-strand breaks in irradiated yeast cells. Int J Radiat Biol Relat Stud Phys Chem Med 1979; 36:261–70.
18. Georgakilas AG, Bennett PV, Wilson DM, 3rd, Sutherland BM. Processing of bistranded abasic DNA clusters in gamma-irradiated human hematopoietic cells. Nucleic Acids Res 2004; 32:5609–20.
19. Sutherland BM, Bennett PV, Sidorkina O, Laval J. Clustered damages and total lesions induced in DNA by ionizing radiation: oxidized bases and strand breaks. Biochemistry 2000; 39:8026–31.
20. Sutherland BM, Bennett PV, Sidorkina O, Laval J. Clustered DNA damages induced in isolated DNA and in human cells by low doses of ionizing radiation. Proc Natl Acad Sci U S A 2000; 997:103–8.
21. Sutherland BM, Bennett PV, Sutherland JC, Laval J. Clustered DNA damages induced by X rays in human cells. Radiat Res 2002; 157:611–6.
22. Hada M, Georgakilas AG. Formation of clustered DNA damage after high-LET irradiation: a review. J Radiat Res (Tokyo) 2008; 49:203–10.
23. Sutherland BM, Georgakilas AG, Bennett PV, Laval J, Sutherland JC. Quantifying clustered DNA damage induction and repair by gel electrophoresis, electronic imaging and number average length analysis. Mutat Res 2003; 531:93–107.
24. Sonntag C, SpringerLink (Online service). Free-radical-induced DNA damage and its repair a chemical perspective. Berlin, Heidelberg: Springer-Verlag; 2006. Available from: http://dx.doi.org/10.1007/3-540-30592-0.
25. Wallace SS. Enzymatic processing of radiation-induced free radical damage in DNA. Radiat Res 1998; 150 Suppl:S60–79.
26. Georgakilas AG. Processing of DNA damage clusters in human cells: current status of knowledge. Mol Biosyst 2008; 4:30–5.
27. Jackson SP. Sensing and repairing DNA double-strand breaks. Carcinogenesis 2002; 25:687–96.
28. Jeggo PA. The fidelity of repair of radiation damage. Radiat Prot Dosimetry 2002; 99:117–22.
29. Rothkamm K, Kruger I, Thompson LH, Lobrich M. Pathways of DNA double-strand break repair during the mammalian cell cycle. Mol Cell Biol 2003; 23:5706–15.
30. Shrivastav M, De Haro LP, Nickoloff JA. Regulation of DNA double-strand break repair pathway choice. Cell Res 2008; 18:134–47.
31. Frankenberg D, Frankenberg-Schwager M, Blocher D, Harbich R. Evidence for DNA double-strand breaks as the critical lesions in yeast cells irradiated with sparsely or densely ionizing radiation under oxic or anoxic conditions. Radiat Res 1981; 88:524–32.
32. Hirayama R, Furusawa Y, Fukawa T, Ando K. Repair kinetics of DNA-DSB induced by X-rays or carbon ions under oxic and hypoxic conditions. J Radiat Res (Tokyo) 2005; 46:325–32.
33. Jenner TJ, deLara CM, O'Neill P, Stevens DL. Induction and rejoining of DNA double-strand breaks in V79-4 mammalian cells following gamma- and alpha-irradiation. Int J Radiat Biol 1993; 64:265–73.
34. Nygren J, Ahnstrom G. The oxygen effect in permeabilized and histone-depleted cells: an enhanced OER for DNA double-strand breaks, compared to single-strand breaks, is abolished by soluble scavengers. Int J Radiat Biol 1997; 72:163–70.
35. Prise KM, Folkard M, Davies S, Michael BD. Measurement of

DNA damage and cell killing in Chinese hamster V79 cells irradiated with aluminum characteristic ultrasoft X rays. Radiat Res 1989; 117:489–99.

36. Prise KM, Folkard M, Davies S, Michael BD. The irradiation of V79 mammalian cells by protons with energies below 2 MeV. Part II. Measurement of oxygen enhancement ratios and DNA damage. Int J Radiat Biol 1990; 58:261–77.

37. Whitaker SJ, McMillan TJ. Oxygen effect for DNA double-strand break induction determined by pulsed-field gel electrophoresis. Int J Radiat Biol 1992; 61:29–41.

38. Pinto M, Prise KM, Michael BD. Evidence for complexity at the nanometer scale of radiation-induced DNA DSBs as a determinant of rejoining kinetics. Radiat Res 2005; 164:73–85.

39. Radford IR. DNA lesion complexity and induction of apoptosis by ionizing radiation. Int J Radiat Biol 2002; 78:457–66.

40. Ward JF. The complexity of DNA damage: relevance to biological consequences. Int J Radiat Biol 1994; 66:427–32.

41. Darroudi F, Natarajan AT, van der Schans GP. Biochemical and cytogenetical characterization of Chinese hamster ovary X-ray-sensitive mutant cells xrs 5 and xrs 6. VI. The correlation between UV-induced DNA lesions and chromosomal aberrations, and their modulations with inhibitors of DNA repair synthesis. Mutat Res 1990; 235:129–35.

42. Prosser JS, White CM, Edwards AA. The effect of oxygen concentration on the X-ray induction of chromosome aberrations in human lymphocytes. Mutat Res 1979; 61:287–95.

43. Barendsen GW, Koot CJ, Van Kersen GR, Bewley DK, Field SB, Parnell CJ. The effect of oxygen on impairment of the proliferative capacity of human cells in culture by ionizing radiations of different LET. Int J Radiat Biol Relat Stud Phys Chem Med 1966; 10:317–27.

44. Barendsen GW, Walter HM. Effects of different ionizing radiations on human cells in tissue culture. IV. Modification of radiation damage. Radiat Res 1964; 21:314–29.

45. Furusawa Y, Fukutsu K, Aoki M, Itsukaichi H, Eguchi-Kasai K, Ohara H, et al. Inactivation of aerobic and hypoxic cells from three different cell lines by accelerated ^{3}He-, ^{12}C- and ^{20}Ne-ion beams. Radiat Res 2000; 154:485–96.

46. Gerweck LE, Richards B, Jennings M. The influence of variable oxygen concentration on the response of cells to heat or X irradiation. Radiat Res 1981; 85:314–20.

47. Koch CJ, Kruuv J, Frey HE. Variation in radiation response of mammalian cells as a function of oxygen tension. Radiat Res 1973; 53:33–42.

48. Ling CC, Michaels HB, Gerweck LE, Epp ER, Peterson EC. Oxygen sensitization of mammalian cells under different irradiation conditions. Radiat Res 1981; 86:325–40.

49. Ling CC, Spiro IJ, Mitchell J, Stickler R. The variation of OER with dose rate. Int J Radiat Oncol Biol Phys 1985; 11:1367–73.

50. Michaels HB, Epp ER, Ling CC, Peterson EC. Oxygen sensitization of CHO cells at ultrahigh dose rates: prelude to oxygen diffusion studies. Radiat Res 1978; 76:510–21.

51. Murray D, Macann A, Hanson J, Rosenberg E. ERCC1/ERCC4 5′-endonuclease activity as a determinant of hypoxic cell radiosensitivity. Int J Radiat Biol 1996; 69:319–27.

52. Palcic B, Skarsgard LD. Reduced oxygen enhancement ratio at low doses of ionizing radiation. Radiat Res 1984; 100:328–39.

53. Sapora O, Barone F, Belli M, Maggi A, Quintiliani M, Tabocchini MA. Relationships between cell killing, mutation induction and DNA damage in X-irradiated V79 cells: the influence of oxygen and DMSO. Int J Radiat Biol 1991; 60:467–82.

54. Shridhar R, Estabrook W, Yudelev M, Rakowski J, Burmeister J, Wilson GD, et al. Characteristic 8 keV X rays possess radiobiological properties of higher-LET radiation. Radiat Res 2010; 173:290–7.

55. Skarsgard LD, Harrison I. Dose dependence of the oxygen enhancement ratio (OER) in radiation inactivation of Chinese hamster V79-171 cells. Radiat Res 1991; 127:243–7.

56. Spiro IJ, Ling CC, Stickler R, Gaskill J. Oxygen radiosensitisation at low dose rate. Br J Radiol 1985; 58:357–63.

57. Watts ME, Hodgkiss RJ, Jones NR, Fowler JF. Radiosensitization of Chinese hamster cells by oxygen and misonidazole at low X-ray doses. Int J Radiat Biol Relat Stud Phys Chem Med 1986; 50:1009–21.

58. Semenenko VA, Stewart RD. A fast Monte Carlo algorithm to simulate the spectrum of DNA damages formed by ionizing radiation. Radiat Res 2004; 161:451–7.

59. Barkas WH, Evans DA. Nuclear research emulsions. New York: Academic Press; 1963.

60. Emfietzoglou D, Nikjoo H. Accurate electron inelastic cross sections and stopping powers for liquid water over the 0.1–10 keV range based on an improved dielectric description of the Bethe surface. Radiat Res 2007; 167:110–20.

61. Hsiao Y, Stewart RD. Monte Carlo simulation of DNA damage induction by x-rays and selected radioisotopes. Phys Med Biol 2008; 53:233–44.

62. Reniers B, Liu D, Rusch T, Verhaegen F. Calculation of relative biological effectiveness of a low-energy electronic brachytherapy source. Phys Med Biol 2008; 53:7125–35.

63. ICRU. Microdosimetry. Bethesda (Maryland): International Commission of Radiation Units and Measurements; 1983. Report No. 36.

64. Kellerer AM. Chord-length distributions and related quantities for spheriods. Radiat Res 1984; 98:425–37.

65. Kellerer AM, Chmelevsky D. Criteria for the applicability of LET. Radiat Res 1975; 63:226–34.

66. Prise KM, Davies S, Michael BD. A comparison of the chemical repair rates of free radical precursors of DNA damage and cell killing in Chinese hamster V79 cells. Int J Radiat Biol 1992; 61:721–8.

67. Prise KM, Davies S, Michael BD. Evidence for induction of DNA double-strand breaks at paired radical sites. Radiat Res 1993; 134:102–6.

68. Dasu A, Denekamp J. New insights into factors influencing the clinically relevant oxygen enhancement ratio. Radiother Oncol 1998; 46:269–77.

69. Dasu A, Denekamp J. Superfractionation as a potential hypoxic cell radiosensitizer: prediction of an optimum dose per fraction. Int J Radiat Oncol Biol Phys 1999; 43:1083–94.

70. Jones B, Dale RG. Mathematical models of tumour and normal tissue response. Acta Oncol 1999; 38:883–93.

71. Nahum AE, Movsas B, Horwitz EM, Stobbe CC, Chapman JD. Incorporating clinical measurements of hypoxia into tumor local control modeling of prostate cancer: implications for the alpha/beta ratio. Int J Radiat Oncol Biol Phys 2003; 57:391–401.

72. Orton CG. In regard to Nahum et al. (Int J Radiat Oncol Biol Phys 2003; 57:391–401): Incorporating clinical measurements of hypoxia into tumor control modeling of prostate cancer: implications for the alpha/beta ratio. Int J Radiat Oncol Biol Phys 2004; 58:1637; author reply 1639.

73. Wouters BG, Brown JM. Cells at intermediate oxygen levels can be more important than the ‘‘hypoxic fraction’’ in determining tumor response to fractionated radiotherapy. Radiat Res 1997; 147:541–50.

74. Carlson DJ, Stewart RD, Li XA, Jennings K, Wang JZ, Guerrero M. Comparison of in vitro and in vivo alpha/beta ratios for prostate cancer. Phys Med Biol 2004; 49:4477–91.

75. Koch CJ. A thin-film culturing technique allowing rapid gas-liquid equilibration (6 sec) with no toxicity to mammalian cells. Radiat Res 1984; 97:434–42.

76. Bortfeld T. An analytical approximation of the Bragg curve for therapeutic proton beams. Med Phys 1997; 24:2024–33.
77. Kramer M, Jakel O, Haberer T, Kraft G, Schardt D, Weber U. Treatment planning for heavy-ion radiotherapy: physical beam model and dose optimization. Phys Med Biol 2000; 45:3299–317.
78. Alloni D, Campa A, Belli M, Esposito G, Facoetti A, Friedland W, et al. A Monte Carlo study of the radiation quality dependence of DNA fragmentation spectra. Radiat Res 2010; 173:263–71.
79. Campa A, Alloni D, Antonelli F, Ballarini F, Belli M, Dini V, et al. DNA fragmentation induced in human fibroblasts by ^{56}Fe ions: experimental data and Monte Carlo simulations. Radiat Res 2009; 171:438–45.
80. Lobrich M, Cooper PK, Rydberg B. Non-random distribution of DNA double-strand breaks induced by particle irradiation. Int J Radiat Biol 1996; 70:493–503.
81. Ratnayake RK, Semenenko VA, Stewart RD. Retrospective analysis of double-strand break rejoining data collected using warm-lysis PFGE protocols. Int J Radiat Biol 2005; 86:421–8.
82. Cedervall B, Kallman P, Dewey WC. Repair of DNA double-strand breaks: errors encountered in the determination of half-life times in pulsed-field gel electrophoresis and neutral filter elution. Radiat Res 1995; 142:23–8.
83. Semenenko VA, Stewart RD. Monte Carlo simulation of base and nucleotide excision repair of clustered DNA damage sites. II. Comparisons of model predictions to measured data. Radiat Res 2005; 164:194–201.
84. Semenenko VA, Stewart RD, Ackerman EJ. Monte Carlo simulation of base and nucleotide excision repair of clustered DNA damage sites. I. Model properties and predicted trends. Radiat Res 2005; 164:180–93.
85. Nikjoo H, Bolton CE, Watanabe R, Terrissol M, O'Neill P, Goodhead DT. Modelling of DNA damage induced by energetic electrons (100 eV to 100 keV). Radiat Prot Dosimetry 2002; 99:77–80.
86. Nikjoo H, Lindborg L. RBE of low energy electrons and photons. Phys Med Biol 2010; 55:R65–109.
87. Nikjoo H, O'Neill P, Goodhead DT, Terrissol M. Computational modelling of low-energy electron-induced DNA damage by early physical and chemical events. Int J Radiat Biol 1997; 71:467–83.
88. Nikjoo H, O'Neill P, Terrissol M, Goodhead DT. Quantitative modelling of DNA damage using Monte Carlo track structure method. Radiat Environ Biophys 1999; 38:31–8.
89. Nikjoo H, O'Neill P, Wilson WE, Goodhead DT. Computational approach for determining the spectrum of DNA damage induced by ionizing radiation. Radiat Res 2001; 156:577–83.
90. Friedland W, Jacob P, Bernhardt P, Paretzke HG, Dingfelder M. Simulation of DNA damage after proton irradiation. Radiat Res 2003; 159:401–10.
91. de Lara CM, Hill MA, Jenner TJ, Papworth D, O'Neill P. Dependence of the yield of DNA double-strand breaks in Chinese hamster V79-4 cells on the photon energy of ultrasoft X rays. Radiat Res 2001; 155:440–8.
92. Kuhne M, Urban G, Frankenberg D, Lobrich M. DNA double-strand break misrejoining after exposure of primary human fibroblasts to C_K characteristic X rays, 29 kVp X rays and ^{60}Co gamma rays. Radiat Res 2005; 164:669–76.
93. Frankenberg D, Goodhead DT, Frankenberg-Schwager M, Harbich R, Bance DA, Wilkinson RE. Effectiveness of 1.5 keV aluminium K and 0.3 keV carbon K characteristic X-rays at inducing DNA double-strand breaks in yeast cells. Int J Radiat Biol Relat Stud Phys Chem Med 1986; 50:727–41.
94. Frankenberg D. Interpretation of the dose and LET dependence of RBE values for lethal lesions in yeast cells. Radiat Res 1984; 97:329–40.
95. Botchway SW, Stevens DL, Hill MA, Jenner TJ, O'Neill P. Induction and rejoining of DNA double-strand breaks in Chinese hamster V79-4 cells irradiated with characteristic aluminum K and copper L ultrasoft X rays. Radiat Res 1997; 148:317–24.
96. Belli M, Cherubini R, Dalla Vecchia M, Dini V, Esposito G, Moschini G, et al. DNA fragmentation in V79 cells irradiated with light ions as measured by pulsed-field gel electrophoresis. I. Experimental results. Int J Radiat Biol 2002; 78:475–82.
97. Kiefer J, Egenolf R, Ikpeme S. Heavy ion-induced DNA double-strand breaks in yeast. Radiat Res 2002; 157:141–8.
98. Jenner TJ, Belli M, Goodhead DT, Ianzini F, Simone G, Tabocchini MA. Direct comparison of biological effectiveness of protons and alpha-particles of the same LET. III. Initial yield of DNA double-strand breaks in V79 cells. Int J Radiat Biol 1992; 61:631–7.
99. Yokota Y, Yamada S, Hase Y, Shikazono N, Narumi I, Tanaka A, et al. Initial yields of DNA double-strand breaks and DNA fragmentation patterns depend on linear energy transfer in tobacco BY-2 protoplasts irradiated with helium, carbon and neon ions. Radiat Res 2007; 167:94–101.
100. Newman HC, Prise KM, Michael BD. The role of higher-order chromatin structure in the yield and distribution of DNA double-strand breaks in cells irradiated with X-rays or alpha-particles. Int J Radiat Biol 2000; 76:1085–93.
101. Hoglund E, Blomquist E, Carlsson J, Stenerlow B. DNA damage induced by radiation of different linear energy transfer: initial fragmentation. Int J Radiat Biol 2000; 76:539–47.
102. Rydberg B, Heilbronn L, Holley WR, Lobrich M, Zeitlin C, Chatterjee A, et al. Spatial distribution and yield of DNA double-strand breaks induced by 3–7 MeV helium ions in human fibroblasts. Radiat Res 2002; 158:32–42.
103. Ikpeme S, Lobrich M, Akpa T, Schneider E, Kiefer J. Heavy ion-induced DNA double-strand breaks with yeast as a model system. Radiat Environ Biophys 1995; 34:95–9.
104. Fakir H, Sachs RK, Stenerlow B, Hofmann W. Clusters of DNA double-strand breaks induced by different doses of nitrogen ions for various LETs: experimental measurements and theoretical analyses. Radiat Res 2006; 166:917–27.
105. Radulescu I, Elmroth K, Stenerlow B. Chromatin organization contributes to non-randomly distributed double-strand breaks after exposure to high-LET radiation. Radiat Res 2004; 161:1–8.
106. Esposito G, Belli M, Campa A, Cherubini R, Cuttone G, Dini V, et al. DNA fragments induction in human fibroblasts by radiations of different qualities. Radiat Prot Dosimetry 2006; 122:166–8.
107. Belli M, Campa A, Dini V, Esposito G, Furusawa Y, Simone G, et al. DNA fragmentation induced in human fibroblasts by accelerated ^{56}Fe ions of differing energies. Radiat Res 2006; 165:713–20.
108. Dini V, Antonelli F, Belli M, Campa A, Esposito G, Simone G, et al. Influence of PMMA shielding on DNA fragmentation induced in human fibroblasts by iron and titanium ions. Radiat Res 2005; 164:577–81.